Geophys. J. Int. (1993) **113,** 419–433

Geomagnetic field models incorporating frozen-flux constraints

Catherine G. Constable,[1] Robert L. Parker[1] and Philip B. Stark[2]

[1] *Institute of Geophysics and Planetary Physics, Scripps Institution of Oceanography, La Jolla, Ca 92093, USA*
[2] *Department of Statistics, University of California, Berkeley, Ca 94720, USA*

Accepted 1992 October 1. Received 1992 August 13; in original form 1991 October 17

SUMMARY

Techniques for modelling the geomagnetic field at the surface of Earth's core often penalize contributions at high spherical harmonic degrees to reduce the effect of mapping crustal fields into the resulting field model at the core–mantle boundary (CMB). Ambiguity in separating the observed field into crustal and core contributions makes it difficult to assign error bounds to core field models, and this makes it hard to test hypotheses that involve pointwise values of the core field. The frozen-flux hypothesis, namely that convective terms dominate diffusive terms in the magnetic-induction equation, requires that the magnetic flux through every patch on the core surrounded by a zero contour of the radial magnetic field remains constant, although the shapes, areas and locations (but not the topology) of these patches may change with time. Field models exactly satisfying the conditions necessary for the hypothesis have not yet been constructed for the early part of this century. We show that such models must exist, so testing the frozen-flux hypothesis becomes the question of whether the models satisfying it are geophysically unsatisfactory on other grounds, for example because they are implausibly rough or complicated. We introduce an algorithm to construct plausible field models satisfying the hypothesis, and present such models for epochs 1945.5 and 1980.

Our algorithm is based on a new parametrization of the field in terms of its radial component B_r at the CMB. The model consists of values of B_r at a finite set of points on the CMB, together with a rule for interpolating the values to other points. The interpolation rule takes the specified points to be the vertices of a spherical triangle tessellation of the CMB, with B_r varying linearly in the gnomonic projections of the spherical triangles onto planar triangles in the planes tangent to the centroids of the spherical triangles. This parametrization of B_r provides a direct means of constraining the integral invariants required by the frozen-flux hypothesis.

Using this parametrization, we have constructed field models satisfying the frozen-flux hypothesis for epochs 1945.5 and 1980, while fitting observatory and survey data for 1945.5 and Magsat data for 1980. We use the better constrained 1980 CMB field model as a reference for 1945.5: we minimize the departure of the 1945.5 CMB field model from a regularized 1980 CMB field model, while constraining the 1945.5 model to have the same null-flux curves and flux through those curves as the 1980 model. The locations, areas and shapes of the curves are allowed to change. The resulting 1945.5 CMB field model is nearly as smooth as that for 1980, fits the data adequately, and satisfies the conditions necessary for the frozen-flux hypothesis.

Key words: frozen-flux model, geomagnetic field, Magsat data.

1 INTRODUCTION

During the past decade several new techniques for modelling the Earth's magnetic field and its secular variation have been introduced. Their development has been spurred by the availability of new satellite data with excellent spatial coverage (Langel 1989); the best data are those from Magsat in 1980. In attempts to understand the temporal evolution of

the field, the newer modelling techniques have been applied to satellite, survey and observatory data extending back to the middle of the seventheenth century (Bloxham, Gubbins & Jackson 1989; Hutcheson & Gubbins 1990). Geomagnetic field models at the core–mantle boundary (CMB) are usually constructed by downward continuation of the surface potential field under the assumption that the mantle is a non-magnetic insulator. Constructing CMB field models is the first step in the more complicated problem of modelling the fluid motion in Earth's core. The geomagnetic models are treated as data for the fluid-flow problem. Flow models are intrinsically non-unique, and it has become customary to restrict the model space by making assumptions about the nature of the flow. Many flow models are constructed under the frozen-flux hypothesis (Roberts & Scott 1965), which supposes that on short time intervals diffusion can be neglected. The model space may be reduced further by seeking steady flows (Voorhies & Backus 1985), geostrophic flows (Backus & Le Mouël 1986) or toroidal flows (Lloyd & Gubbins 1990). Bloxham & Jackson (1991) provide a review of core-flow models.

Here we test whether a set of observatory and survey data for 1945.5 and Magsat data for 1980 are compatible with the frozen-flux hypothesis. It is to be expected that at sufficiently small spatial scales there will be diffusive effects; the question is whether surface and satellite geomagnetic observations have the resolution to detect such effects. Booker (1969) argued that there was little evidence for diffusion in 1965 secular variation models, and Benton, Estes & Langel (1987) have constructed models satisfying the frozen-flux hypothesis for 1980. However, Bloxham & Gubbins (1985, 1986) have asserted that there is evidence for flux diffusion over as short a time span as the last two decades. Their result depends on uncertainty estimates for the radial core field, which are used to assess the significance of differences in flux through null-flux curves (contours on which the radial magnetic field is zero) at different epochs. Models have since been constructed that satisfy a subset of the frozen-flux constraints for all but the early part of this century (Bloxham *et al.* 1989). The conditions not satisfied concern null flux-curve topology, which is not generally believed to engender a strong violation of the frozen-flux hypothesis. Radial core fields that are consistent with the available data for the first quarter of this century, and at the same time satisfy even the restricted subset of frozen-flux constraints not involving topology, have yet to be constructed. We show here that for any pair of epochs field models exist that satisfy arbitrary sets of data and the necessary conditions for the frozen-flux hypothesis; the question is whether any such pairs of models are plausible, or whether they are all unreasonably complicated.

Procedures to model the geomagnetic field at the CMB usually penalize high spatial frequencies (see for examples, Shure, Parker & Backus 1982; Shure, Parker & Langel 1985; Gubbins 1983; Gubbins & Bloxham 1985; Bloxham & Gubbins 1985, 1986). This penalty, often known as regularization, gives models that minimize a quantitative measure of roughness while fitting data to an appropriate tolerance. The justifications for regularization and the particular measures of roughness vary, but all tend to reduce artefacts due to the crustal field in the CMB field models. Ambiguity in separating the crustal field from the core field makes it impossible to put useful pointwise error bounds on CMB field models without making what some regard as excessively restrictive presumptions about the statistical structure of the core field (see Backus 1987, 1988, 1989). Error bounds can be determined for certain averages of the field, such as individual spherical harmonic coefficients, using Backus' (1989) confidence set inference and Stark's (1992) minimax procedures, under the simplifying assumption that noise in the measurements (including any crustal and external fields) is not spatially correlated. Crustal fields are better understood now than they used to be (Langel *et al.* 1988; Jackson 1990), but there remains a fundamental ambiguity in separating crustal and core contributions to the measured field.

There are infinitely many CMB field models compatible with the available data; the fact that some features may be shared by many models [in particular, regularized models of the type reviewed by Bloxham *et al.* (1989)] makes it tempting to conclude that those features are required by the data, and hence likely to be shared by the true field. However, the similarities might be caused by common aspects of the modelling algorithms, rather than the physics and the measurements. Similarly, it is probably unwise to conclude from such models that changes from one epoch to the next are necessary properties of the field, particularly when data of very variable types and quality are used at different epochs. It is necessary to distinguish between identifying interesting, unusual or persistent features in CMB field models, and testing whether those features are necessary to explain the observations. The first activity involves constructing plausible models of the field; the second concerns making inferences about the field from the data, often by testing hypotheses suggested by the plausible models.

Here we address an inference problem, developing another solution to the construction problem along the way. We show that the frozen-flux hypothesis cannot be rejected on the basis of an extensive set of observatory and survey data for 1945.5 and 1980 Magsat data; we do this by constructing models that both satisfy the frozen-flux conditions and adequately fit the data. If, on the other hand, we had proved that no reasonable models exist that satisfy the necessary conditions and fit the data, we could have rejected the frozen-flux hypothesis.

We present an algorithm to construct of pairs of field models at different epochs consistent with the frozen-flux hypothesis. We impose constraints on core field models using a new parametrization of the radial field at the CMB. We use the better constrained 1980 field model as a reference for 1945.5, and require null-flux curves in the 1980 model to appear in the 1945.5 model with the same integrated flux, but allow their shapes, areas and positions to differ in the two epochs. We analysed the available magnetic data statistically to determine appropriate misfit levels for the observatory and survey data. The resulting 1945.5 model is almost as smooth as the 1980 model based on Magsat data, fits the data adequately, and is compatible with the frozen-flux hypothesis. Thus while Bloxham & Gubbins (1985) have suggested that there are indications of significant diffusion during this time period, the 1945.5 and 1980 data do not require the frozen-flux hypothesis to be violated.

2 A NEW PARAMETRIZATION FOR THE GEOMAGNETIC FIELD ON THE CORE: SPHERICAL TRIANGLE TESSELATION

We parametrize the geomagnetic field in terms of the radial magnetic field, B_r, at the CMB. The radial field over the sphere defining the core surface specifies (up to a constant) the potential from which the field components can be computed anywhere outside the core (see Appendix). The justification for this is the uniqueness theorem for the solution of the exterior Neumann boundary value problem for Laplace's equation (see e.g. Mikhlin 1970, p. 270). The individual surface field components are given in terms of $B_r(\hat{s})$,the radial field on the core surface, S, by

$$B_r(\boldsymbol{r}) = \frac{1}{4\pi}\int_S d^2\hat{s} B_r(\hat{s})\left[\frac{\rho^2(1-\rho^2)}{R^3} - \rho^2\right] \tag{1}$$

$$B_\theta(\boldsymbol{r}) = -\frac{1}{4\pi}\int_S d^2\hat{s}\,\frac{B_r(\hat{s})}{R^3}\left[\frac{1+2R-\rho^2}{T}\right]\rho^3\hat{s}\cdot\hat{\theta} \tag{2}$$

$$B_\phi(\boldsymbol{r}) = -\frac{1}{4\pi}\int_S d^2\hat{s}\,\frac{B_r(\hat{s})}{R^3}\left[\frac{1+2R-\rho^2}{T}\right]\rho^3\hat{s}\cdot\hat{\phi} \tag{3}$$

where

$$\rho = \frac{c}{r}, \qquad \mu = \hat{r}\cdot\hat{s} \tag{4}$$

$$R = \sqrt{1-2\mu\rho+\rho^2}, \qquad T = 1+R-\mu\rho. \tag{5}$$

Here $\hat{r}$ is the unit vector in the direction of the measurement location, $\hat{s}$ is a unit vector ranging over the core surface, and c is the core radius. $\hat{\theta}$ and $\hat{\phi}$ are local directions at the measurement site, pointing southward and eastward. Our models for the field on the CMB are specified in terms of the radial field at the vertices of spherical triangles forming a tessellation covering the surface of the core. At intermediate points the field is defined by a linear interpolation for B_r within the gnomonic projection of each spherical triangle onto a plane tangent at its centroid. This interpolation scheme replaces the one implied by the basis of spherical harmonics usually used to represent B_r. The major advantage of this representation is that it provides a simple framework within which to impose direct constraints on such things as integral invariants of frozen flux.

A triangular tessellation of 360 points is shown in Fig. 1 in Hammer–Aitoff equal-area projection, often incorrectly called Aitoff's projection; see Snyder & Voxland (1989). The model points are chosen to be approximately evenly distributed over the core surface. In Fig. 1 they have an average angular separation of 10°. Most of the models described in this paper were constructed using a set of 788 model points, with average angular separation of 7°. An advantage of this parametrization is that in areas of particular interest we can place a much denser array of model points without the computational expense of providing additional points in other regions. It should be obvious that the tessellation of spherical triangles connecting the model points is not unique. We have chosen the Delaunay tesselation on the spherical surface (see Rogers 1964); this has the property that the resulting triangles are as nearly equi-angular as possible. The tessellation on the sphere is constructed using our modification of an algorithm by Watson (1982) for finding Delaunay tessellations from points distributed over a plane. Each point in the model is assigned an index, the tessellation is then specified by a list of the triplets forming the vertices of each triangle. For a tessellation of N points there are $2N-4$ triangles. The integrals specified in eqs (1)–(3) are thus reduced to

$$B_r(\boldsymbol{r}) = \frac{1}{4\pi}\sum_{i=1}^{2N-4}\int_{\Delta_i} d^2\hat{s} B_r(\hat{s})\left[\frac{\rho^2(1-\rho^2)}{R^3} - \rho^2\right] \tag{6}$$

$$B_\theta(\boldsymbol{r}) = -\frac{1}{4\pi}\sum_{i=1}^{2N-4}\int_{\Delta_i} d^2\hat{s}\,\frac{B_r(\hat{s})}{R^3}\left[\frac{1+2R-\rho^2}{T}\right]\rho^3\hat{s}\cdot\hat{\theta} \tag{7}$$

$$B_\phi(\boldsymbol{r}) = -\frac{1}{4\pi}\sum_{i=1}^{2N-4}\int_{\Delta_i} d^2\hat{s}\,\frac{B_r(\hat{s})}{R^3}\left[\frac{1+2R-\rho^2}{T}\right]\rho^3\hat{s}\cdot\hat{\phi}. \tag{8}$$

The integral over each spherical triangle is performed numerically. The triangle is first projected onto the plane tangent at its circumcentre using a gnomonic projection. Great circles are projected as straight lines, and so the spherical triangles become planar triangles in the map plane. The integral over the planar triangle is then approximated by a weighted sum of samples of the

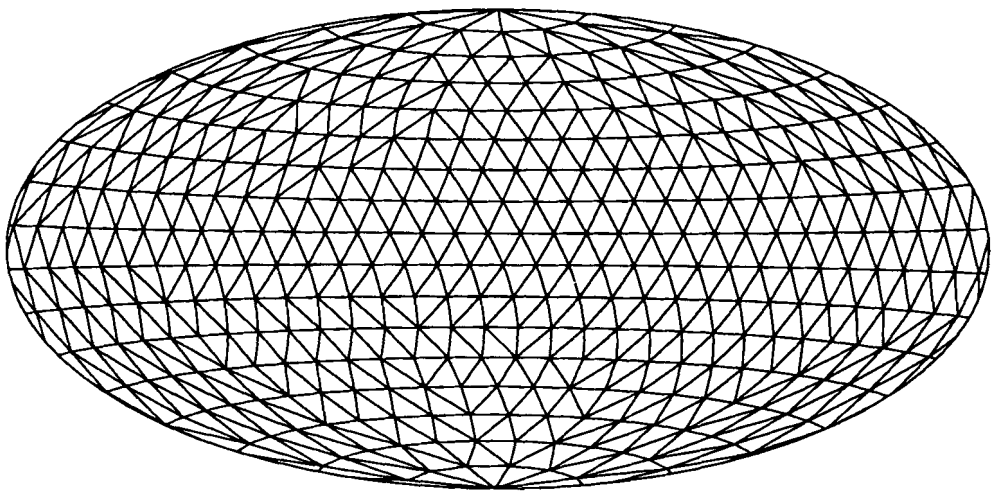

Figure 1. Hammer–Aitoff equal-area projection showing the 360-point spherical triangle tessellation on the core surface.

appropriate function

$$\int_\Delta f(\hat{s})d^2\hat{s} \approx \sum_j w_j f(\hat{s}_j). \tag{9}$$

We use Stroud's (1971, p. 314) optimal degree-5 cubature rule for triangular regions to supply the w_j. It uses seven sample points inside the triangle and is exact for all polynomial functions in the plane with degree less than or equal to 5. The field, $B_r(\hat{s})$, is specified at the vertices of our spherical triangle tessellation (STT). We define its value at points within and along the boundaries of the triangles using the following linear interpolation scheme. Suppose

$$\hat{s}_j = \alpha_1\hat{x}_1 + \alpha_2\hat{x}_2 + \alpha_3\hat{x}_3 \tag{10}$$

where $\hat{x}_1, \hat{x}_2, \hat{x}_3$ are model points forming the vertices of the spherical triangle containing the point $\hat{s}_j$, and $\alpha_1 + \alpha_2 + \alpha_3 = 1$, with $\alpha_i \geq 0$. Then $B_r(\hat{s}_j)$ is derived in precisely the same way from the function values at those vertices. i.e.

$$B_r(\hat{s}_j) = \alpha_1 B_r(\hat{x}_1) + \alpha_2 B_r(\hat{x}_2) + \alpha_2 B_r(\hat{x}_3). \tag{11}$$

Because linear interpolation on the common edge of neighbouring triangles yields the same field in either triangle, the interpolated function is continuous everywhere.

Using this relationship in eq. (9), eqs (1)–(3) can be written in the form

$$d = Gb \tag{12}$$

where b is now a vector of radial magnetic field values at the tessellation points on the CMB, d is a vector of observations of geomagnetic elements at various observation sites, and G is the matrix representing eqs of the type (1)–(3). Since the interpolation rule is linear, the cubature rule is exact for flux integrals of STT models.

3 FINDING SMOOTH SPHERICAL TRIANGLE TESSELLATION MODELS

In constructing core field models we follow the philosophy of Shure *et al.* (1982) and find the unique model that minimizes some property of the field measuring roughness or complexity, subject to satisfying the data at an appropriate misfit level. The solution of the downward continuation problem then reduces to finding the minimum over b of the functional

$$U = \left\{\sum_{i=1}^{n}\left[\frac{\mathcal{G}_i(b) - d_i}{\sigma_i}\right]^2 - T\right\} + \lambda\mathcal{F}(b) \tag{13}$$

where $\mathcal{G}_i$ is the forward functional relating the field model b to the surface or satellite field at the position of d_i, the ith measurement, σ_i is the uncertainty (one standard deviation) associated with measurement d_i, T is the desired misfit level, and $\mathcal{F}(b)$ is a function measuring size or roughness of b. For the orthogonal field components, B_r, B_θ and B_ϕ, the forward function $\mathcal{G}_i$ is linear and corresponds to the ith row of the matrix G defined implicitly in (12). However, if inclination or intensity measurements are used directly, $\mathcal{G}_i$ will be non-linear. The size of the Lagrange multiplier λ adjusts the trade off between smoothness of the model and misfit to the data. We choose it so that the rms misfit level is the expected value of χ^2, i.e.

$$\sum_{i=1}^{n}\left[\frac{\mathcal{G}_i(b) - d_i}{\sigma_i}\right]^2 = n. \tag{14}$$

A variety of functions $\mathcal{F}$ may be used, such as the integrated squared radial field over the CMB, the integrated squared-horizontal gradient of the radial field, or approximations to heat-flow constraints. The effect of minimizing these functions (while fitting the data to the required tolerance) is predominantly to provide models for B_r that have little power at small spatial scales and so they are smooth solutions; we think of such models as possessing minimal complexity in the sense defined by the particular form of $\mathcal{F}$. Evaluating $\mathcal{F}$ involves integrals over the surface of the core of functionals of the radial core field model; thus, the constraint term can be readily evaluated using a numerical scheme of the kind described above. The value of λ required to satisfy (14) is not known *a priori* so (13) must be minimized a number of times, with a succession of trial values. The correct value of λ is the one achieving the target misfit level and we apply a numerical scheme to refine the values and home in on the proper solution. When $\mathcal{G}_i$ is linear the treatment of eq. (13) for a field model b follows closely that described by Constable & Parker (1988) for a similar type of problem.

For two special forms of $\mathcal{F}$ we have been able to speed the algorithm considerably by making an approximation to the relevant integrals. Instead of summing the integrals over spherical triangles (which involves the gnomonic projection), we approximate them by integrals over planar triangles. Suppose we are interested in finding the model that minimizes the $\mathcal{F}_2$ norm of Shure *et al.* (1982).

$$\mathcal{F}_2 = \int_S B_r^2 d^2\hat{s}.$$

If $f(\boldsymbol{x})$ varies linearly over the plane triangle T and takes the values f_1, f_2, and f_3 at the vertices of T, then

$$\int_T f(\boldsymbol{x})^2 d^2\boldsymbol{x} = \frac{\Delta}{6}(f_1^2 + f_2^2 + f_3^2 + f_1f_2 + f_1f_3 + f_2f_3)$$

where Δ = area of T.
Similarly, the $\mathcal{F}_4$ norm of Shure *et al.* is

$$\mathcal{F}_4 = \int_S |\nabla_s B_r|^2 \, d^2\hat{s}.$$

If the gradient of f is constant on T, then

$$\int_T |\nabla f|^2 \, d^2\boldsymbol{x} = \frac{1}{4\Delta}[s_1^2f_1^2 + s_2^2f_2^2 + s_3^2f_3^2 + f_1f_2(s_3^2 - s_1^2 - s_2^2) + f_1f_3(s_2^2 - s_1^2 - s_3^2) + f_2f_3(s_1^2 - s_2^2 - s_3^2)].$$

We have applied the penalty using the interpolation scheme on a polyhedral core; the numerical result is essentially identical to doing the full interpolation on spherical triangles. This might be expected, since we don't really care about the exact values of B_r or ∇B_r in this situation, but only about the integral of their squares.

In order to assess our new parametrization technique, we repeated work carried out earlier by Shure *et al.* (1985). They used selected Magsat data to generate a preliminary harmonic spline model (PHS) for 1980; their model found

the field, B_r, at the CMB that minimized the integrated squared radial field on the core surface, subject to fitting the data to within $10\,nT$ rms. We used the same data set and constraints to find a model for B_r. The positions of null-flux curves (lines on which $B_r = 0$) on the CMB are readily found by looking for changes in the sign of B_r between neighbouring points. The PHS model is compared with our spherical triangle tessellation model, STT 80, in Fig. 2, and the two appear remarkably similar. Both are plotted at a core radius $c = 3485$ km, as are the other CMB models discussed later. One extremely small null-flux curve seen in PHS 80 is absent in the tessellation model; we attribute this to our use of planar triangles in the regularization of the STT modelling, resulting in a slightly stronger roughness penalty than $\int_S B_r^2 d^2\hat{s}$, because the core radius is effectively underestimated in most places. The flux through the remaining curves is similar, as is the total unsigned flux (37 380 MWb for PHS and 37 082 MWb for STT 80; see Table 2). Although the linear interpolation used in STT 80 results in a model that appears a little less smooth spatially than PHS, the STT model has slightly smaller roughness when the norm is calculated exactly for a spherical core surface rather than the polyhedral core. The difference in B_r at model points for PHS 80 and STT 80 ranged between -18.4 and $20.0\,\mu T$, with an rms deviation of $6.5\,\mu T$ (about 2 per cent of the rms model values of $300\,\mu T$). This is much smaller than the differences we found between models constructed with alternative regularization constraints; e.g. there was a $28.5\,\mu T$ rms difference between models constructed using the $\mathcal{F}_2$ and $\mathcal{F}_4$ norms. We infer that the differences are due to the small difference in roughness measure used in the two modelling procedures. This is supported by the fact that when a smaller number of parameters (360 model points) is used in the STT model, resulting in a stronger roughness penalty, the rms difference increases to $26.4\,\mu T$.

STT 80 and PHS 80 fit the data equally well, and we have no reason for regarding one kind of representation as superior to the other, except that, as we shall see, the STT representation helps us to construct models consistent with the frozen-flux hypothesis. The spherical harmonic representation of the STT model can easily be computed by integration of the field against the spherical harmonics. In common with the harmonic spline field representation, STT models can have infinite degree spherical harmonic representations. However, the imposition of a regularization constraint (such as the integrated squared field used here) forces the higher order terms to decrease in size rapidly, and an extremely accurate spherical harmonic representation can be obtained by degree 20. Although STT models are not strictly speaking continuously differentiable at the triangle boundaries, the degree 20 spherical harmonic expansion of the STT model is infinitely differentiable and satisfies both the data and constraints. The results shown in Fig. 2 give us confidence that the spherical triangle tessellation of radial field points on the surface of the core provides a useful framework for modelling the geomagnetic field on the CMB.

4 DATA SETS FOR 1945 AND 1980

A case that we have studied extensively is a comparison of the field in 1945 with 1980. The data available for these two epochs are substantially different in type. The 1980 field is modelled using the subset of Magsat data described above, while the available measurements for 1945 consist of permanent magnetic observatory data and survey measurements (and are the same data discussed by Langel *et al.* 1988 in finding the DGRF for 1945). The satellite measurements are influenced much less by the crustal component to Earth's magnetic field and are more accurate and more uniform in spatial distribution than the 1945 measurements. The rms misfit to the data of $10\,nT$ used in the PHS model is probably reasonable; the measurement uncertainties are around $6\,nT$ according to Langel & Estes (1985) and crustal contribution is probably 5–$10\,nT$ rms at Magsat altitudes, thus it would certainly be extremely optimistic to require a misfit of much less than $10\,nT$.

In contrast to the recent satellite measurements, the observatory and survey data from 1945 are strongly influenced by crustal magnetization. At permanent observatories we corrected for this effect by applying the bias corrections discussed and tabulated by Langel *et al.* (1988), but uncertainties in these corrections and the generally lower precision of the measurements make the resulting data less accurate than those collected by Magsat. The bias corrections used for observatories cannot be obtained for survey data as the corrections rely on continuous measurement of the field over long periods of time.

The survey data set, fully described by Langel *et al.* (1988), comprises scattered observations of all the conventional geomagnetic elements measured with a variety of portable instruments. For the purposes of this paper we selected a five-year time interval from the middle of 1942 to the middle of 1947 from which to construct a data set focusing on 1945.5. This interval contained 16,261 observations. While it would not be inconceivable with today's computer resources to treat every one of these measurements as a separate datum for our magnetic model, there are good reasons. for not doing this. The most important one is that the observations are extremely concentrated into a few locations (such as Scandinavia and Central Europe). When crustal signals are considered to be noise sources, as they are in our analysis, observations made even hundreds of kilometers apart must not be treated as possessing statistically independent noise components but this is what happens if the data are entered separately in the misfit term of (13); then sites of very high observation density would attract unrealistically good agreement from the model. Our solution, the same one adopted by other investigators, is to make estimates of representative values within zones large enough that correlation of the crustal perturbations is negligible. Before such local values can be formed, however, the observations must be adjusted and edited in several ways.

We are fortunate in having the excellent geomagnetic field models of earlier workers (especially, Langel *et al.* 1988) from which to begin our work; our flux-conserving solution cannot deviate far from these standards or it could not be in accord with observation. First the effects of secular variation were corrected for by applying a linear time correction based on models of Langel *et al.* (1988). The deviation of each element from its 1945.5 value was found by linear interpolation in the 1945 and 1950 models; this deviation was then subtracted from the observed element, correcting it

back to 1945.5. The effects of this correction are comparatively slight in terms of the overall misfit level, but at the small number of survey sites where repeated observations had been made in the interval, there was usually a reduction in scatter.

The kinds of observations made at an individual site varied considerably. For example, there were 9267 observation sites at which only declination D was recorded, but the data set contained no measurements of the magnetic elements X, Y or F. Rather than fitting the actual elements recorded at the various sites, we decided to construct whenever possible the elements X, Y and Z from the observations of H, I and D; we also accepted D when it appeared alone and Z was also observed at some sites. The fitted elements X, Y and Z can all be written in terms of linear functionals of the radial magnetic field at the CMB [eqs (6), (7) and (8)]; misfit to D can also be transformed into a linear condition through the variable

$$C = X_m \sin D - Y_m \cos D = 0 \tag{15}$$

where X_m and Y_m are model predictions of the magnetic elements X and Y. If the model matches the observed value of D, then C is zero; this condition can be included in (13) by adding C^2 suitably weighted into the quadratic misfit functional. In this way we completely avoid the need to solve a non-linear fitting problem, at the expense of reducing the measurement pool from 16261 numbers to 15097.

Having formed the basic data set, we next carried out a screening process to remove aberrant values. Using the DGRF1945 model as the standard, we plotted histograms and QQ plots of the residuals of the magnetic elements and the quantity C, defined in (15). QQ plots (Barnett & Lewis 1984) give a graphical representation of the distribution of the noise and indicate the deviation from a Gaussian distribution. The quadratic misfit measure used in (13) may be badly biased if the noise statistics deviate far from the ideal Gaussian pattern, particularly if the deviations take the form of large outliers. A simple resolution of the problem is to delete data that fall many standard deviations away from the standard, since their presence distorts the solution, and is almost certainly due to processes other than crustal fields, which appear roughly Gaussian in distribution (Jackson 1990). We note that C in (15) is much more nearly Gaussian in its behaviour than D, which has a heavy-tailed distribution produced by large swings in the neighbourhood of the magnetic poles; thus C is a superior variable statistically as well as being simpler to fit because of its linear relation to the field model. A total of 21 outlying data were removed from the set by this screening. That this number is so small is an indication of the careful editing the data had already received during the compilation of the data set.

The next task is to generate representative values of the field in regions about five degrees in diameter. Having captured a number of observations of a particular magnetic element in a region, it would not be correct simply to average the values, since a bias is introduced by the curvature of the main field. This is easily seen at a local maximum (say the maximum for Z near the north magnetic pole); averaging the values in a zone centred on the local maximum would give a downward bias since all observations would fall below the peak value. The solution to the difficulty again involves the standard model DGRF1945. Deviations from the standard were averaged, and the mean deviation was added to the predicted value at the representative location for the region. The representative location was the centre of mass of the observations in the region, treating each measurement site as a unit point mass.

Table 1. Data used for 1945.5 field modelling.

Data Type	No. of points	standard deviation (nT)
Observatory		
X	59	50
Y	59	45
Z	58	65
Survey		
X	496	110
Y	495	107
Z observed	172	202
Z calculated	404	192
D	322	124

Table 1 lists the type and number of data used in our modelling, along with their assigned uncertainties. Those for the observatory measurements include a contribution due to uncertainty in the bias corrections given by Langel *et al.* (1988). The data distribution is illustrated in the maps in Figs 3, 4 and 5.

Fig. 6(a) and (b) show regularized models for B_r at the CMB for the Magsat data (STT 80) and the 1945.5 geomagnetic survey and observatory data (STT 45). The same inversion procedure and regularization penalty have been applied to each, i.e. minimize

$$\left(\sum_{i=1}^{n} \left[\frac{\mathcal{G}_i(b) - d_i}{\sigma_i} \right]^2 - T \right) + \lambda \int_S B_r^2 d^2 r \tag{16}$$

with λ chosen so that the rms misfit level is the expected value of χ^2, i.e. to satisfy (14).

The integrated squared radial field over the surface of the core is similar for the two models ($1.10 \times 10^{12}\, nT^2$ for 1980 and $1.02 \times 10^{12}\, nT^2$ for 1945.5) as is the total unsigned flux. There are, however, some apparently large differences in B_r on the CMB; STT 80 has eight null flux curves, while STT 45 field has only six. The flux through each patch surrounded by a null flux curve is listed in Table 2, where we have named the patches according to the conventions used by Bloxham *et al.* (1989). The large bone-shaped patch in 1980 appears to have been formed by the joining of two patches from the earlier epoch. An obvious question to ask is whether the changing null-flux curves represent a necessary violation of the frozen-flux condition, or whether they reflect our inability to resolve the core field variations because of differences in the type, distribution and quality of the data. Note that we have achieved a unique model by placing stringent penalties on the kind of model that is acceptable. If lack of resolution is the cause of the differences from the 1980 solution then it should be possible to find models at each epoch satisfying the data to within the desired misfit level but with the same integral invariants of frozen flux. In the next section we describe an algorithm for constructing such a model.

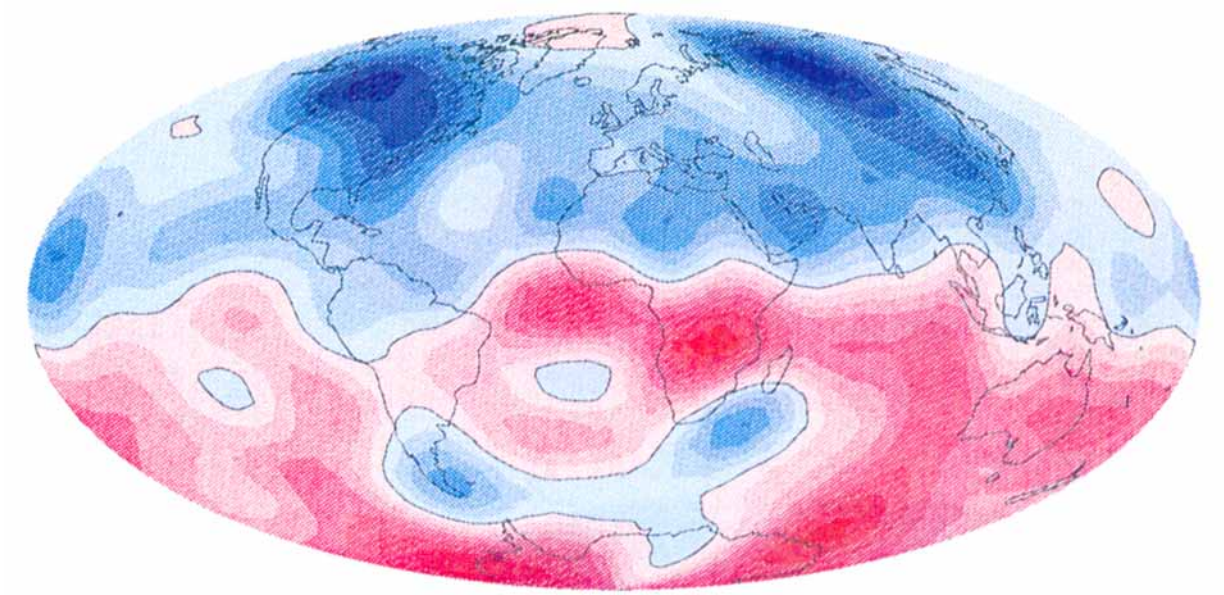

STT 1980 rms=1.00

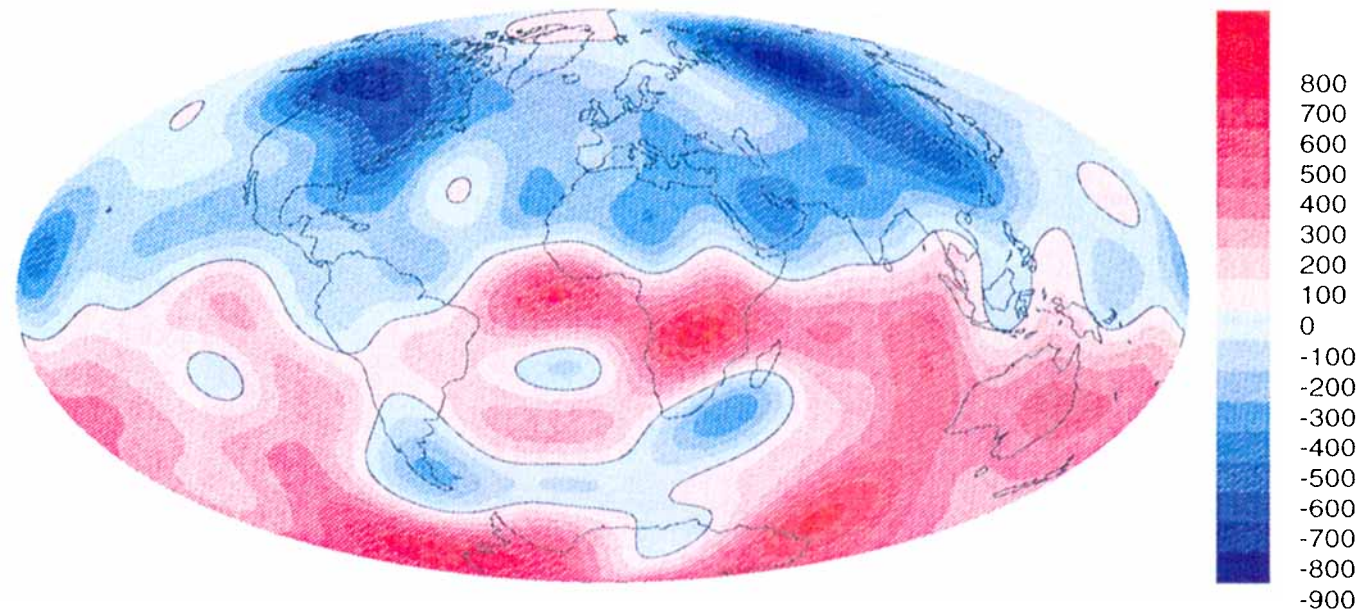

PHS 1980 rms=1.00

Figure 2. Comparison of the preliminary harmonic spline model for 1980 with the spherical triangle tessellation model for the same epoch. All models are plotted at core radius $c = 3485$ km.

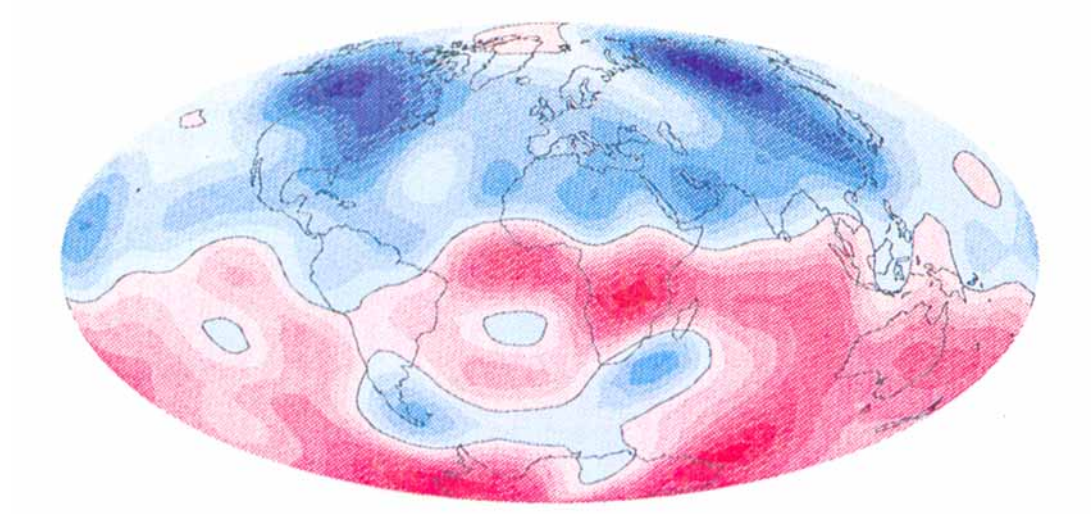

(a) STT 1980 rms=.998

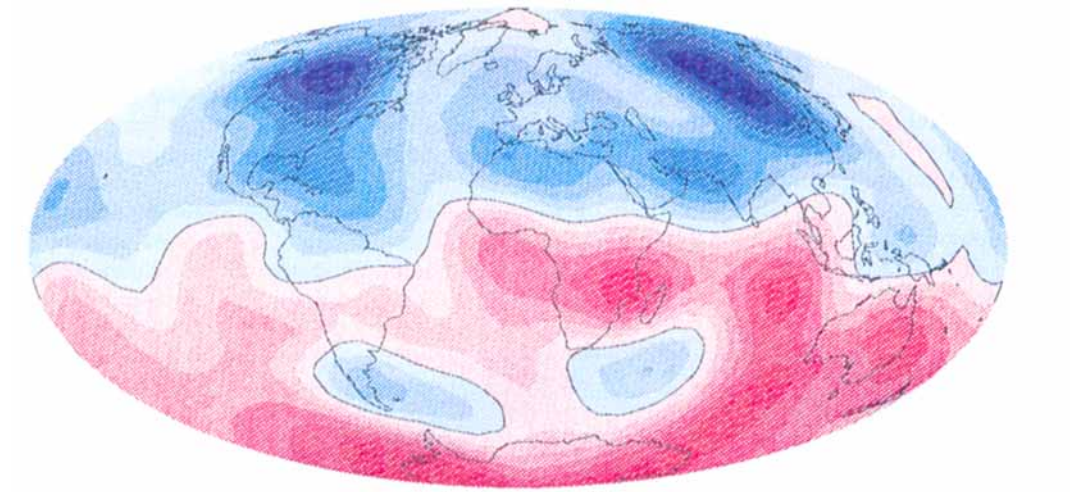

(b) STT 1945 rms=1.023

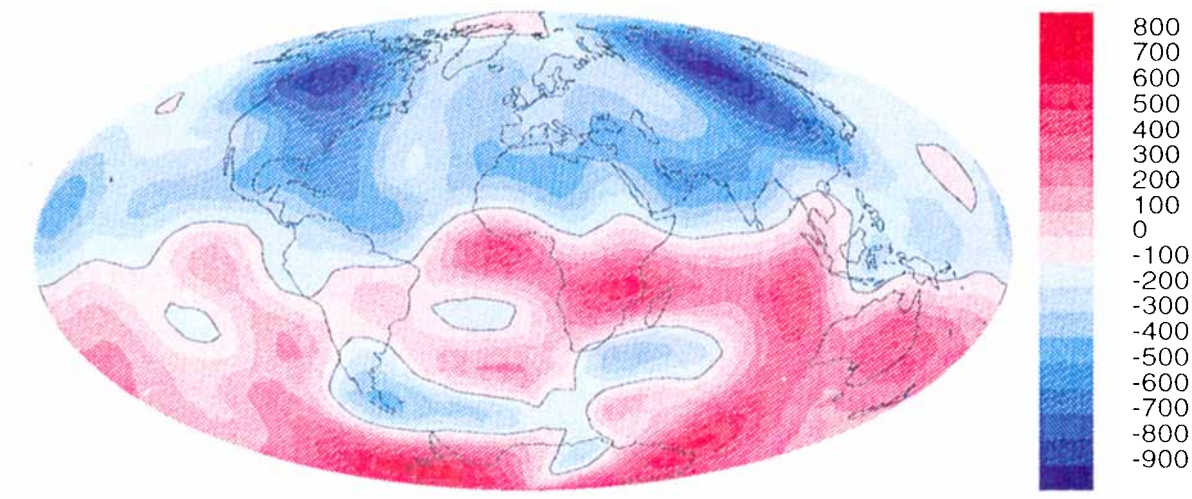

Figure 6. Spherical triangle tessellation models for 1945.5 and 1980. STT 80 and STT 45 were constructed using a penalty on the integrated squared radial field. STT 45 FF is constrained to have the same number of null-flux patches as STT 80 and the same integrated flux through equivalent patches.

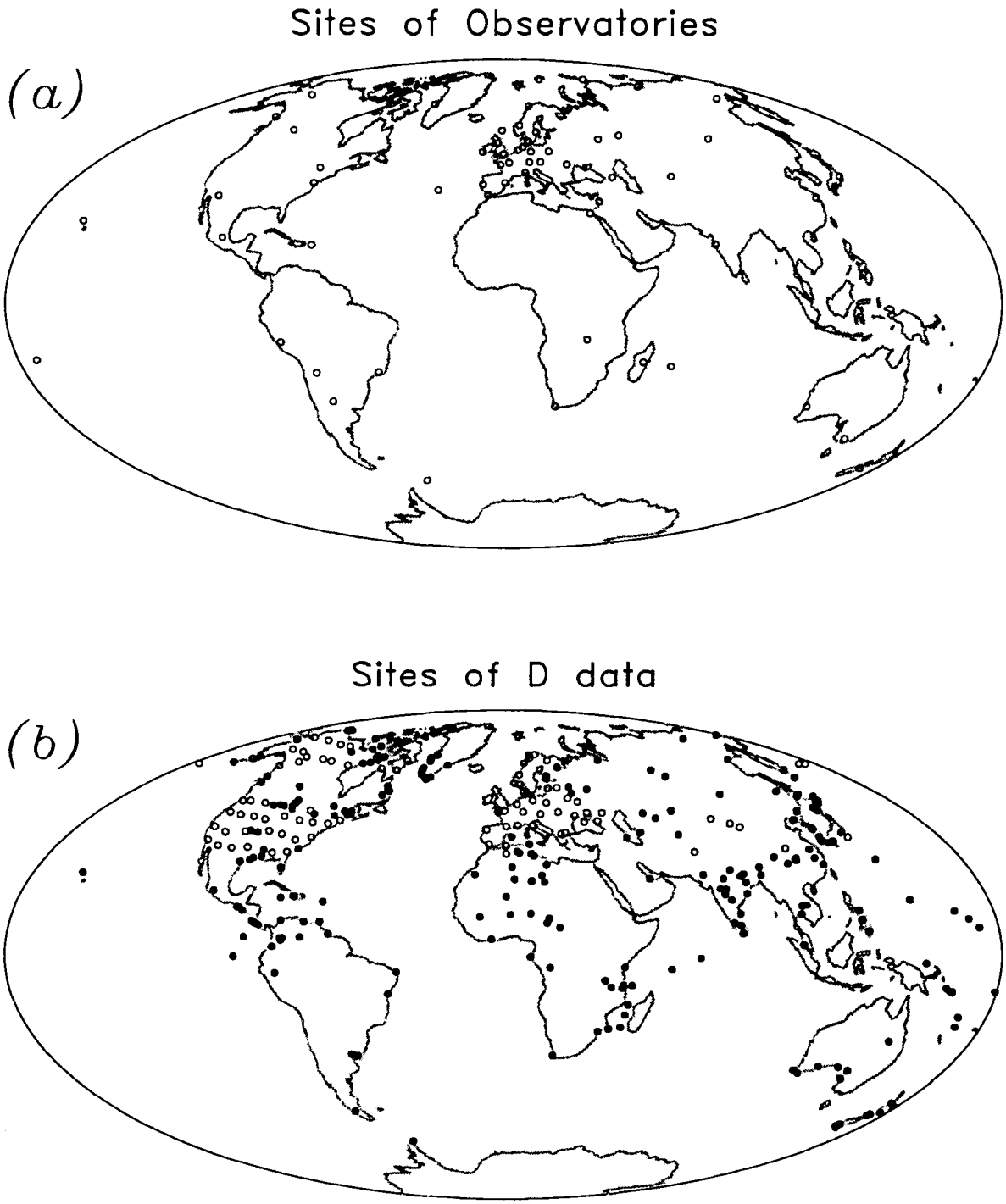

Figure 3. (a) Sites of the geomagnetic observatories used in this work; each observatory contributes X, Y and Z magnetic elements to the data pool. (b) Sites of magnetic survey declination data used in this work; an open circle denotes the site of a single observation of D, a solid dot a site at which several measurements were combined as described in the text. Only those D values not used in the calculation of X and Y are shown here.

5 FROZEN FLUX MODELS

The magnetic field variations in Earth's core are described by the magnetic induction equation

$$\frac{\partial \boldsymbol{B}}{\partial t} = \eta \nabla^2 \boldsymbol{B} + \nabla \times (\boldsymbol{u} \times \boldsymbol{B}) \tag{17}$$

with $\boldsymbol{B}$ the magnetic field, t time, $\boldsymbol{u}$ fluid velocity, $\eta = \frac{1}{\mu_0 \sigma}$ magnetic diffusivity. The magnetic Reynolds number, $R_m = \frac{UL}{\eta}$, with U and L representing typical velocity and length scales, is a measure of the relative importance of field changes due to convection and diffusion. $R_m \gg 1$ implies the dominance of convective field changes. Roberts & Scott (1965) noted that the time scales for diffusion, $\tau_d =$

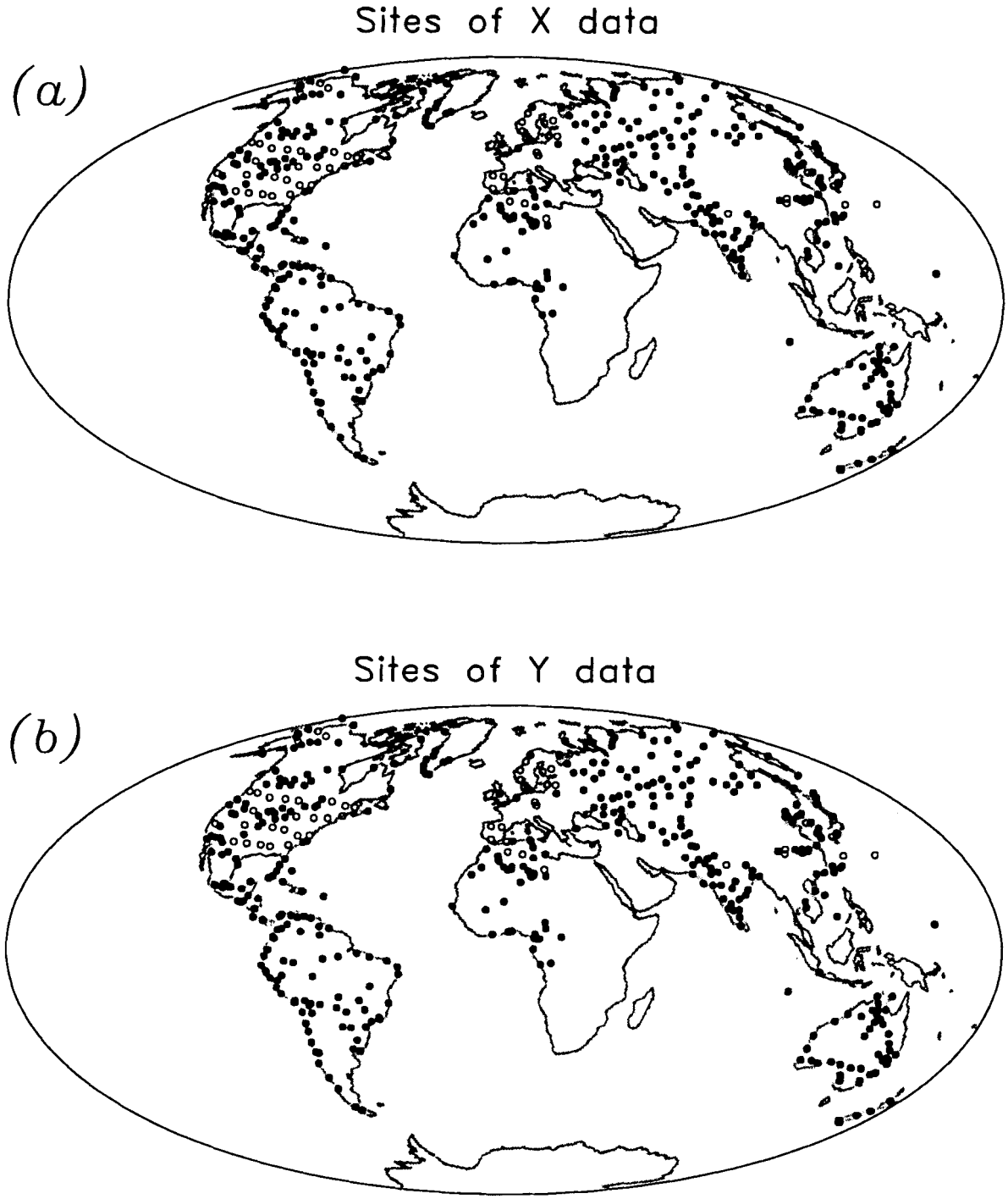

Figure 4. (a) Sites of X data used in this work; X was computed by combining the elements D and H measured in magnetic surveys. An open circle denotes the site of a single survey station; a solid dot a site at which several results were combined. (b) As in (a) but for the magnetic element Y.

$\frac{L^2}{\eta}$, can be expected to be much longer than those for advection, $\tau_u = \frac{L}{U}$, given the high electrical conductivity in the core. They suggested that diffusion has a negligible effect on secular variation over time scales shorter than 10^2 yr so that the magnetic induction equation can be approximated by

$$\frac{\partial \boldsymbol{B}}{\partial t} = \nabla \times (\boldsymbol{u} \times \boldsymbol{B}). \tag{18}$$

The importance of the frozen-flux hypothesis is that it allows the construction of models of certain kinds of fluid flow in the core from surface field measurements. Making the core

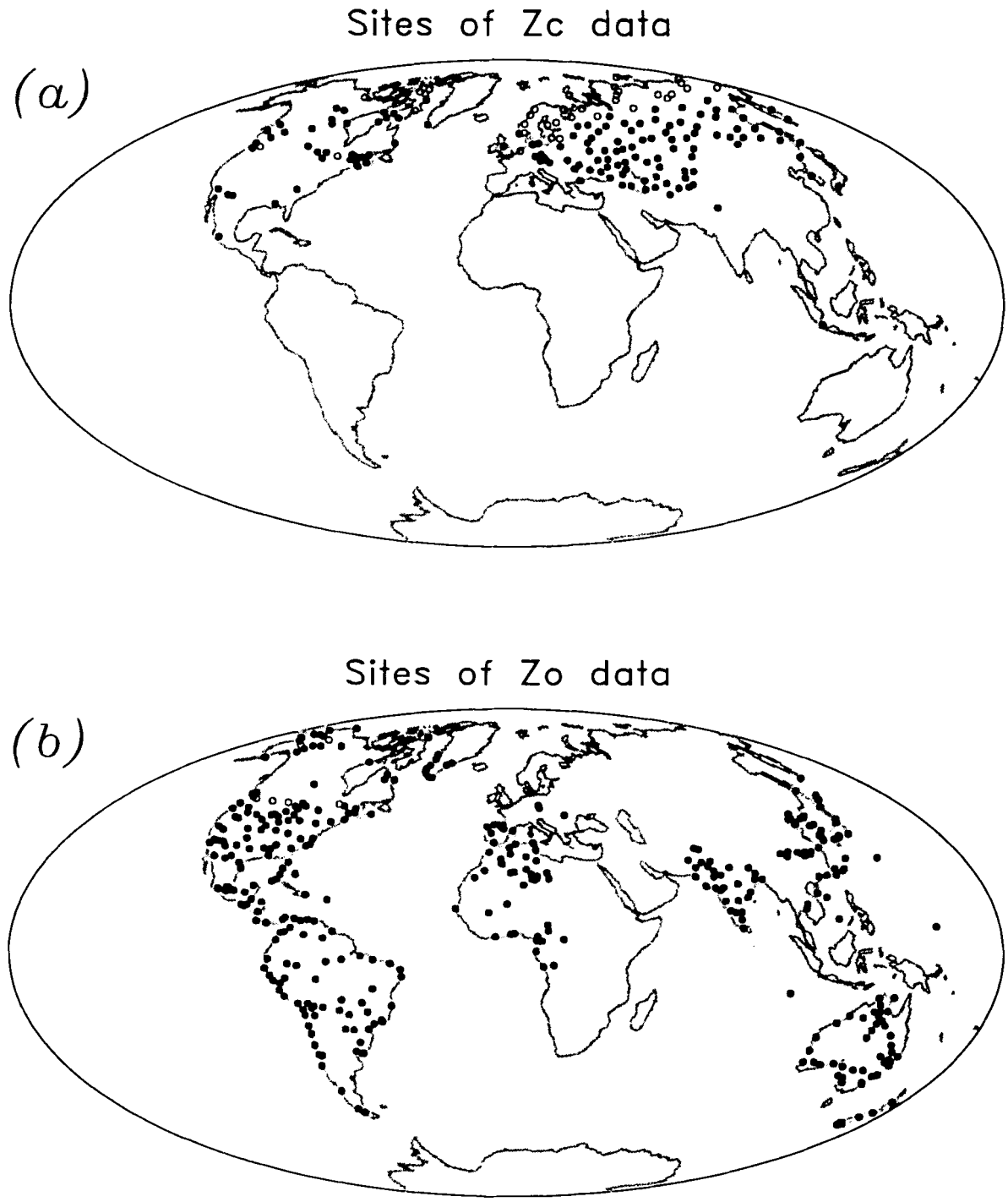

Figure 5. (a) Sites of Z data computed from elements H and I measured in magnetic surveys; open and solid dots have the same meaning as in Fig. 4. (b) Sites of Z data directly measured in magnetic surveys.

surface radial component of velocity zero yields

$$\dot{B}_r + \nabla_s \cdot (\boldsymbol{u} B_r) = 0. \tag{19}$$

The differential eq. (19) does not have a unique solution, so additional constraints are often imposed on $\boldsymbol{u}$. Nonetheless, it remains an important problem to determine over what time scales the frozen-flux approximation holds.

Necessary conditions on the radial magnetic field for the observed secular variation to be consistent with frozen flux were derived by Backus (1968)

$$\int_{S_i} \dot{B}_r d^2\hat{s}_i = 0 \tag{20}$$

where S_i is the ith region on the CMB surrounded by a contour of zero-radial magnetic field. Lines on which $B_r = 0$ are known as null-flux curves. The topology of null-flux curves must also be preserved, although it is generally conceded that very small amounts of diffusion would be

Table 2. Patch flux integrals for PHS80, STT80, STT45 and STT45FF.

	Flux (MWb)			
	PHS80	STT80	STT45	STT45FF
Patch				
North Pole	34.5	39.4	5.8	39.4
North Atlantic	3.2	–	–	–
N. Hemisphere	-17,400	-17,361	-17,175	-17,362
East Pacific	3.7	0.6	–	0.6
West Pacific	17.4	14.1	9.6	14.1
Easter Island	-17.4	-8.1	–	-8.2
St Helena	-53	-34.1	–	-34.1
Bonc	-1170	-1124	-465, -293	-1124
S. Hemisphere	18,630	18,501	17,946	18,501
Total Unsigned Flux	37,380	37,082	35,894	37,084

required for the splitting of a single null-flux curve into two closed curves.

In common with others (see e.g. Bloxham & Jackson 1991) we interpret (20) as the requirement that

$$\frac{d}{dt}\int_{S_i} B_r d^2\hat{s}_i = 0. \tag{21}$$

5.1 Existence of frozen-flux models

Suppose we have two core fields at two distinct epochs t_1 and t_2, where t_1 is the earlier epoch. Then we will believe the second field may have evolved from the first through flux conserving processes if (i) the number of null-flux curves is identical at t_2, (ii) the flux integrals through the null-flux curves, matched together in pairs, is the same for the members of the pairs. We show now that it is always possible to construct field models from magnetic data at two epochs with these properties, provided that we permit arbitrary roughness, that is, very small scale features. The idea is illustrated with a simple example, which can easily be generalized. Consider the two radial field models shown in Fig. 7(a) and (b); negative radial flux is shown shaded. These two models have been constructed to fit the magnetic observations at their epochs. Evidently there are three distinct null-flux curves in model (b), but only one in (a). We may, however, modify (b) by introducing two narrow zones of radial field to connect the formerly isolated minor-flux patches to the appropriate hemispheres as shown in (c). With these narrow bridges in place, model (c) has only one null-flux curve and is topologically equivalent to (a). The introduction of a sufficiently narrow strip of field at the core will have a negligible effect on the values measured at the surface because upward continuation [through (1)–(3)] attenuates the small scale features. Thus as far as observation is concerned, (b) and (c) are indistinguishable. Model (c) satisfies condition (i) above but there is no reason why it should satisfy (ii), the flux integral constraint. Again, the condition can be satisfied by modifying (c) at very small scales as follows. If the flux through the northern hemisphere of (c) is too small compared with the value in (a) we may increase it by introducing a small positive patch with a high normal field just inside the positive boundary, and at the same time placing a small patch with equal and opposite flux just on the other side of the boundary. By employing a pair of patches, we retain the constraint that

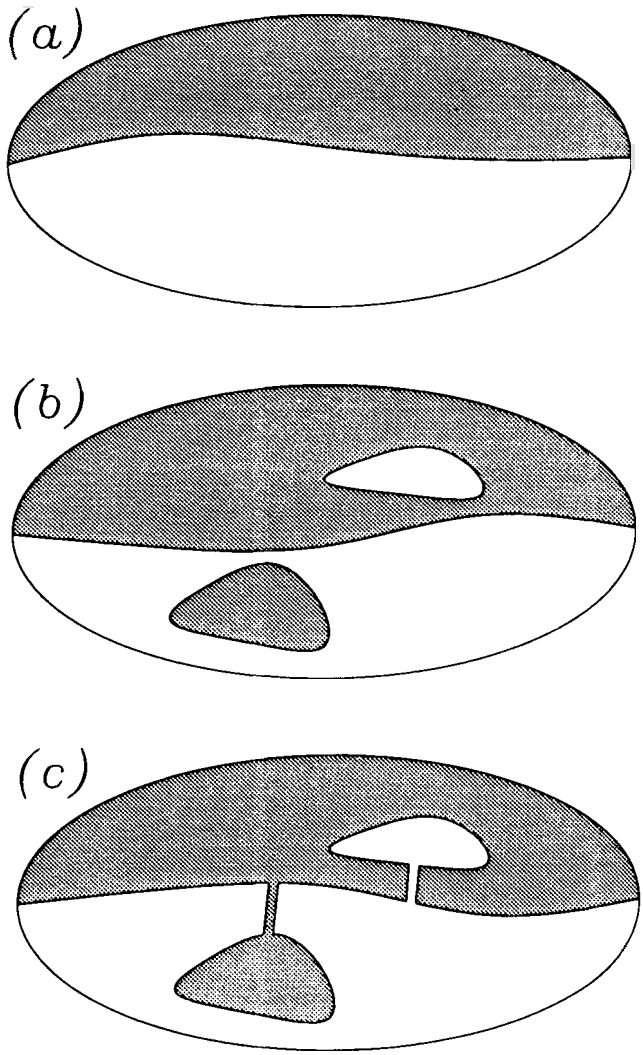

Figure 7. Radial magnetic fields on the surface of the core with regions of negative B_r shaded. (a) and (b) model fields corresponding to two sets of data at different epochs, t_1 and t_2. (c) a slightly modified version of (b) with same number of null-flux curves as in model (a).

the integral of the normal field over the whole core must remain zero. If the flux emerging from the positive patch is made equal to the flux deficit, the new model must now satisfy (ii). It may appear that the observations will no longer be matched by the model, but again, if the patches are made small enough and close enough together, the net field at the surface can be made as small as we please: the key is to keep the moment defined by the product of the separation distance and the flux small, for otherwise a sensible magnetic dipole would develop.

These small-scale perturbations may increase the misfit of the model (c) to its parent data set, making it slightly too large. One way to counter this problem is to build the initial model (b) with a misfit that is slightly too small so that the perturbations raise the level to the proper value. This is always possible if a perfect match to the observation is not demanded, which is invariably the case. Finding a sequence of main field models obeying the conditions of the frozen-flux approximation has been shown to be possible in principle, whatever the data set. Therefore it is incorrect to

claim that magnetic measurements require violation of the approximation. None-the-less if the only solutions in accord with the hypothesis exhibited the kind of intricate and artificial features described here, one would be justified in declaring it implausible. Therefore our approach is to discover by means of regularization, the smoothest solutions obeying the conditions; if these are well behaved, we can say with some force that there is no reason to reject the frozen-flux hypothesis.

5.2 Construction of frozen-flux models

Fig. 6(a) and (b) and Table 2 show that unconstrained models for the field at the CMB do not necessarily have the same number of null-flux patches on the core surface at the epochs 1945.5 and 1980, in violation of the constraint (21) requiring the flux through each patch to remain constant as the field evolves. However, we can construct models that satisfy (21). For our parametrization of the geomagnetic field we can easily find which points in the model are associated with a given patch simply by identifying the sign of B_r at each model point. By virtue of our linear interpolation scheme for B_r on the CMB the integrated flux, $\mathcal{N}_i$ through each patch, S_i, may be written as a vector dot product

$$\mathcal{N}_i = D_i b = \int_{S_i} |B_r(t)|\, d^2\hat{s} \tag{22}$$

with D_i the gradient vector showing how the flux through patch i changes with respect to changes in the model parameters. We must know the field model in order to find which points in the model contribute to a given patch, thus the problem is non-linear. One way to construct a model at an epoch, t_1, that satisfies a given set of p-flux constraints $\mathcal{N}_i(t_1) = \mathcal{N}_i(t_2)$, $i = 1, \ldots p$, in force at epoch t_2 would be to minimize the functional

$$\left[\sum_{j=1}^{n} \left\{\frac{\mathcal{G}_j[b(t_1)] - d_j}{\sigma_j}\right\}^2 - T\right] + \lambda \sum_{i=1}^{p} [\mathcal{N}_i(t_1) - \mathcal{N}_i(t_2)]^2. \tag{23}$$

We chose the 1980 field model as a reference to provide the frozen-flux constraints, $\mathcal{N}_i(t_2)$, that must be matched by the 1945.5 field. The 1980 field model is more detailed and we presume that the greater accuracy and more uniform distribution of the data from which it is constructed make it a closer approximation to the true core field. We then require that every patch present in 1980 must also be found in the constrained 1945.5 field with the same flux through it, and try to construct such a model for 1945.5 consistent with the data. The frozen-flux constraint is non-linear so (23) must be solved iteratively; in practice we found that we needed additional regularization of the model to find a stable solution. The functional we used was to minimize the two norm of the difference between the 1945 and 1980 fields. Thus the objective functional to be minimized is

$$V = \left[\sum_{j=1}^{n} \left\{\frac{\mathcal{G}_j[b(t_1)] - d_j}{\sigma_j}\right\}^2 - T\right] + \lambda \sum_{i=1}^{p} [\mathcal{N}_i(t_1) - \mathcal{N}_i(t_2)]^2 + \nu \, \|b(t_1) - b(t_2)\|^2. \tag{24}$$

Each term in (24) is a quadratic form of the kind minimized in a least-squares problem, since the $\mathcal{N}_i(t_2)$ and $b(t_2)$ may be regarded as data supplied by our reference model at epoch t_2. We begin by finding a smooth model for t_1, using the standard regularization scheme described by eq. (16). This model, denoted $b^0(t_1)$, should ideally fit the data slightly better than the constraint ($\chi^2 = N$) expressed in (14), allowing some flexibility for the imposition of the flux constraints. The null-flux curves in this model are identified and the flux gradient vector D_i^0 calculated for each patch. Where possible each patch at epoch t_1 is identified with a corresponding patch at t_2. Two patches from one epoch may be combined at the other; in such cases we used the topology found in the reference field. If two patches, S_k and S_{k+1} at t_1 corresponded to one at t_2 then the gradient vectors D_k and D_{k+1} were added together to provide a single constraint. Similarly, if one patch at t_1 had split into two at t_2 the patch was split to provide two separate constraints. When patch S_k at time t_1 is not evident at t_2 the corresponding constraint is $\mathcal{N}_k(t_2) = 0$. When a patch is found at t_2, but not at t_1, then a patch is created at t_1 by applying the flux constraint from t_2 to the opposite sign subpatch at t_1 involving the same model points. When this identification system is implemented and the computed flux gradient substituted in (24) we have

$$V = \left[\sum_{j=1}^{n} \left\{\frac{\mathcal{G}_j[b(t_1)] - d_j}{\sigma_j}\right\}^2 - T\right] + \lambda \sum_{i=1}^{p} [D_i^0 b(t_1) - \mathcal{N}_i(t_2)]^2 + \nu \, \|b(t_1) - b(t_2)\|^2 \tag{25}$$

providing an obvious basis for an iterative scheme; i.e. V given by (25) is minimized, yielding $b^1(t_1)$, the new patch configuration and flux gradient vectors are obtained, etc. until a satisfactory model satisfying the flux constraints has been constructed.

The issue of minimizing V is no longer so straightforward as it was for (13); there are now two Lagrange multipliers, yielding more complicated trade offs among misfit to the data, satisfying the flux constraints, and smoothness in the resulting model. One approach is to choose ν so that $b(t_1) - b(t_2)$ is about the size expected from the secular variation difference between the reference model and the starting model $b^0(t_1)$. This works because any reasonable model satisfying the frozen-flux constraints will do for our purposes, and eliminates the need for an extensive and time-consuming search for the optimal trade off between ν and μ.

Using this algorithm it is possible to find models that satisfy the frozen-flux conditions and fit the data to the required tolerance. Such a model is shown in Fig. 6(c), where we compare our constrained model STT 45 FF with the reference model STT 80 and the unconstrained STT 45. The rms misfit (normalized by the data uncertainties) for STT 45 is 1.023 and for STT 45 FF is 1.029, both close to the expected value for χ^2 which corresponds to an rms misfit of 1.000. Table 2 gives the flux through the various patches for all three models. In testing whether the frozen-flux hypothesis is violated, the critical issue is determining reasonable uncertainty estimates for the data. For the 1945 epoch the major contributor is the crustal contribution to the field in the survey data, with standard deviations ranging from 100 to 200 nT depending on which magnetic element is considered (Table 1). The normalized rms misfit achieved by STT 45 and STT 45 FF is comparable to that of Langel *et*

al.'s (1988) definitive IGRF models, which are designed for evaluating the field at Earth's surface and may contain significant crustal contributions. Thus it is likely that our models overfit rather than underfit the data, and a more realistic estimate of data uncertainties might be as much as several times the values we have used. To provide grounds for rejecting the frozen-flux hypothesis we would have to show that for a *reasonable* misfit level to the data, there is no 1945 model that satisfies the constraints. We have shown that even for conservatively small uncertainty estimates the frozen flux constraints are satisfied. Larger uncertainties would only strengthen our case.

We have not had to pay a high cost in terms of increased roughness of the field in order to satisfy the flux constraints. The spatial power spectra at Earth's surface of the resulting models are shown in Fig. 8, where the dashed line is an approximate measure of the crustal contribution to the spectrum, taken from crustal field models by Hahn *et al.* (1984). We use Lowes' (1974) definition of the spectrum,

$$R_l = (l+1)\sum_{m=0}^{l}(g_l^m)^2 + (h_l^m)^2 \tag{26}$$

where the g_l^m's and h_l^m's are the usual Schmidt partially normalized Gauss coefficients in the spherical harmonic expansion for the geomagnetic field. Crustal terms do not begin to dominate the spectrum until beyond about degree 12, and it is clear from the figure that for $l > 12$ the increase in norm resulting from the flux constraints is very small in comparison with the crustal contribution. The rms difference between core model points for STT 80 and STT 45 FF is $69.6\,\mu T$, ranging from -253 to $284\,\mu T$. For the unconstrained STT 45 the rms difference from STT 80 is $108\,\mu T$ (range -438 to $365\,\mu T$). Thus the variations required at the CMB to provide us with the secular variation observed at Earth's surface are only between two and four times as large

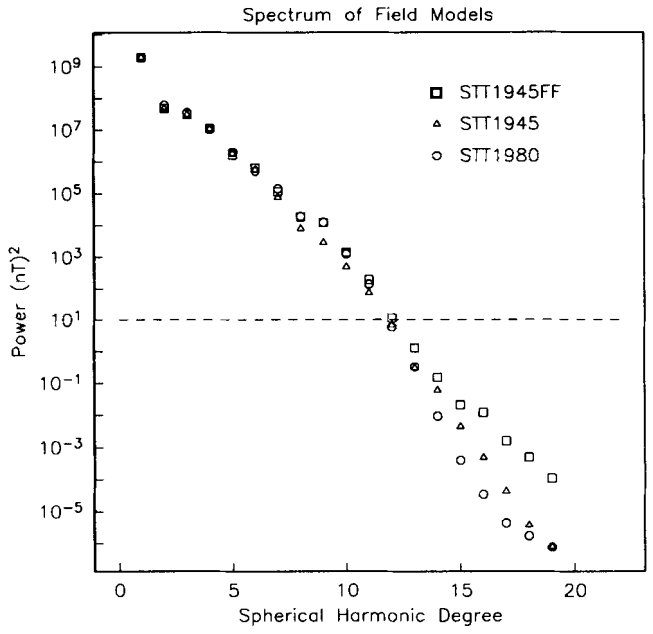

Figure 8. Power spectra of the geomagnetic field at Earth's surface for the models STT 80, STT 45 and STT 45 FF. Dashed line approximates the power in the crustal field.

as the differences found between models constructed under different regularization constraints, such as the $\mathcal{F}_2$ and $\mathcal{F}_4$ norms. It is therefore hardly surprising that by using a different kind of penalty in our modelling algorithm we have been able to show that there is no intrinsic requirement in the 1945.5 and 1980 geomagnetic data sets for the secular variation to violate the frozen-flux hypothesis. This does not necessarily make it valid, but other evidence is needed to infer the existence of detectable diffusive effects.

The success of our hypothesis testing approach on the frozen-flux hypothesis for the 1945.5 and 1980 fields merits its application to other epochs. We chose 1945.5 as a test case because it seemed from the core-field maps previously computed that the time interval was sufficiently long for there to be significant diffusion. In fact the ease with which we were able to construct a frozen-flux model suggests that to resolve diffusion unambiguously we require either a larger effect or a better quality data set.

In the 1950's and 60's there are higher quality, better distributed data available (from satellites, surveys and observatories); prior to 1940 there are extensive survey and observatory measurements, that have been used in obtaining the currently available models (e.g. Bloxham *et al.* 1989). It is unclear which will present the more stringent test to the frozen-flux hypothesis; the older data are less accurate allowing greater tolerance in the misfit level, but the effects of diffusion should be greater the larger the time span covered in comparing models.

Most work on the construction of core field models has involved only the radial field at the core surface. This is because the downward continuation of the horizontal components of magnetization is complicated by the possibility of a discontinuity across the boundary layer between the free stream and the (presumed solid and electrically insulating) mantle. However, theoretical studies show that such a jump should be small (Roberts & Scott 1965; Hide & Stewartson 1972; Braginsky 1984), and Barraclough, Gubbins & Kerridge (1989) estimated that the jump was undetectable using recent frozen-flux models for the field. This would allow the computation of horizontal field components. Backus (1968) derived extended frozen-flux conditions, and if these hold then the horizontal field components may be used to determine the core flow around as well as normal to null-flux curves. The conditions are

$$\frac{d}{dt}\oint_{\partial S_i} Q \cdot dl = 0 \tag{27}$$

where

$$Q = (\boldsymbol{r}\times\boldsymbol{B})\boldsymbol{B}\cdot\nabla(\boldsymbol{r}\cdot\boldsymbol{B}). \tag{28}$$

Barraclough *et al.* found no evidence for violation of these constraints when applied to recent models satisfying the restricted frozen-flux conditions. Lloyd & Gubbins (1990) use the assumption that these extended flux constraints hold in computing toroidal flows at the CMB. These extended frozen-flux constraints can only be computed if there is no surface current in the boundary layer at the top of the core. However, if we accept this, then we can use the hypothesis testing approach to see how far back in time it is possible to construct models satisfying the extended frozen-flux hypothesis.

The key to this work is that the necessary conditions for the frozen-flux hypothesis can be written as integral constraints on the field models satisfying the data. The same is also true for some kinds of flows at the CMB, in particular geostrophic or toroidal flows. We can therefore use the same kind of approach to test whether the geomagnetic data are compatible with these kinds of flows. A major advantage of working with the integral constraints in this case will be that we can really test the hypothesis against the geomagnetic data; algorithms that actually construct flows at the core surface and then assess their properties have been almost exclusively derived from geomagnetic field models (not directly from field measurements), and may be biased by the modelling procedure towards or away from the hypotheses we wish to test.

6 ACKNOWLEDGMENTS

We are extremely grateful to Bob Langel for providing us with Magsat, survey, and observatory data used in this study. This work was funded by NASA grant NAG 5-883, and NSF award DMS 8957573.

REFERENCES

Backus, G. E., 1968. Kinematics of geomagnetic secular variation in a perfectly conducting core, *Phil. Trans. R. Soc. Lond.* A, **263,** 239–266.

Backus, G. E., 1987. Objections to stochastic inversion and Bayesian inference, *EOS,* **68,** 1482.

Backus, G. E., 1988. Bayesian inference in geomagnetism, *Geophys. J. R. astr. Soc.,* **92,** 125–142.

Backus, G. E., 1989. Confidence set inference with a prior quadratic bound, *Geophys. J.,* **97,** 119–150.

Backus, G. E. & Le Mouël, J.-L., 1986. The region on the core–mantle boundary where a geostrophic velocity field can be determined from frozen-flux magnetic data, *Geophys. J.R. astr. Soc.,* **85,** 617–629.

Barnett, V. & Lewis, T., 1984. *Outliers in Statistical Data,* John Wiley, New York.

Barraclough, D., Gubbins, D. & Kerridge, D., 1989. On the use of horizontal components of magnetic field in determining core motions, *Geophys. J. Int.,* **98,** 293–299.

Benton, E. R., Estes, R. H. & Langel, R. A., 1987. Geomagnetic field modelling incorporating constraints from frozen-flux electromagnetism, *Phys. Earth planet. Interiors,* **48,** 241–264.

Bloxham, J. & Gubbins, D., 1985. The secular variation of Earth's magnetic field, *Nature,* **317,** 777–781.

Bloxham, J. & Gubbins, D., 1986. Geomagnetic field analysis—IV. Testing the frozen-flux hypothesis, *Geophys. J.R. astr. Soc.,* **84,** 139–152.

Bloxham, J., Gubbins, D. & Jackson, A., 1989. Geomagnetic secular variation, *Phil. Trans. R. Soc. Lond.,* A, **329,** 415–502.

Bloxham, J. & Jackson, A., 1991. Fluid flow near the surface of Earth's outer core, *Rev. Geophys.,* **29,** 97–120.

Booker, J., 1969. Geomagnetic data and core motions, *Proc. R. Soc. Lond.* A, **309,** 27–40.

Braginsky, S. I., 1984. Short period geomagnetic variations, *Geophys. Astrophys. Fluid Dyn.,* **30,** 1–78.

Constable, C. G. & Parker, R. L., 1988. Smoothing, splines and smoothing splines: their application in geomagnetism, *J. Comp. Physics,* **78,** 493–508.

Gubbins, D., 1983. Geomagnetic field analysis—I. Stochastic inversion, *Geophys. J.R. astr. Soc.,* **73,** 641–652.

Gubbins, D. & Bloxham, J., 1985. Geomagnetic field analysis—III. Magnetic fields on the core–mantle boundary, *Geophys. J.R. astr. Soc.,* **80,** 695–713.

Hahn, A., Ahrendt, H., Meyer, J. & Hufen, J.-H., 1984. A model of magnetic sources within the earth's crust compatible with the field measured by the satellite Magsat, *Geol. Jb.,* **A75,** 125–156.

Hide, R. & Stewartson, K., 1972. Hydromagnetic oscillations of the earth's core, *Rev. Geophys. Space Phys.,* **10,** 579–598.

Hutcheson, K. A. & Gubbins, D., 1990. Earth's magnetic field in the seventeenth century, *J. geophys. Res.,* **95,** 10 769–10 782.

Jackson, A., 1990. Accounting for crustal magnetization in models of the core magnetic field, *Geophys. J. Int.,* **103,** 657–673.

Jackson, J. D., 1963. *Classical Electrodynamics,* John Wiley, New York.

Langel, R. A., 1989. Satellite magnetic measurements. In *Encyclopedia of Solid Earth Geophysics* pp. 977–989, ed. James, D. E., Van Nostrand, Reinhold, New York.

Langel, R. A. & Estes, R. H., 1985 The near-Earth magnetic field at 1980 determined from Magsat data, *J. geophys. Res.,* **90,** 2495–2509.

Langel, R. A., Barraclough, D. R., Kerridge, D. J., Golovkov, V. P., Sabaka, T. J. & Estes, R. H., 1988. Definitive IGRF models for 1945, 1950, 1955, and 1960, *J. Geomagn. Geoelect.,* **40,** 645–702.

Lloyd, D. & Gubbins, D., 1990. Toroidal fluid motion at the top of the Earth's core, *Geophys. J. Int.,* **100,** 455–467.

Lowes, F. J., 1974. Spatial power spectrum of the main geomagnetic field and extrapolation to the core, *Geophys. J.R. astr. Soc.,* **36,** 717–730.

Mikhlin, S. G., 1970. *Mathematical Physics, An Advanced Course,* North-Holland, London.

Roberts, P. H. & Scott, S., 1965. On analysis of the secular variation I. A hydromagnetic constraint, *J. Geomagn. Geoelect.,* **17,** 137–151.

Rogers, C. A., 1964. *Packing and Covering,* Cambridge University Press, Cambridge.

Shure, L., Parker, R. L. & Backus, G. E., 1982. Harmonic splines for geomagnetic modelling, *Phys. Earth planet. Interiors,* **28,** 215–229.

Shure, L., Parker, R. L. & Langel, R. A., 1985. A preliminary harmonic spline model from Magsat data, *J. geophys. Res.,* **90,** 11 505–11 512.

Snyder, J. P. & Voxland, P. M., 1989. *An Album of Map Projections,* US Geological Survey, Professional Paper 1453, US Gov. Printing Office.

Stark, P. B., 1992. Minimax confidence intervals in geomagnetism, *Geophys. J. Int.,* **108,** 329–338.

Stroud, A. H., 1971. *Approximate Calculation of Multiple Integrals,* Prentice-Hall, Englewood Cliffs, NJ.

Voorhies, C. & Backus, G. E., 1985. Steady flows at the top of the core from geomagnetic field models: the steady motions theorem, *Geophys. Astrophys. Fluid Dyn.,* **32,** 163–173.

Watson, D. F., 1982. Acord: automatic contouring of raw data, *Comput. & Geosci.,* **8,** 97–101.

7 APPENDIX: GREEN'S FUNCTION FOR SURFACE MAGNETIC FIELD FROM RADIAL CORE FIELD

The radial magnetic field at a point $\hat{s}$ on the core surface may be represented by a radial source field, $B_r(\hat{s})$,

$$B_r(\hat{s}) = \sum_j \alpha_j b_j(\hat{s}).$$

We use Green's function to find the radial magnetic field at the point $\boldsymbol{r}$ outside Earth's core

$$B_r(\boldsymbol{r}) = \int_S G(\boldsymbol{r} \mid \hat{s}) B_r(\hat{s}) d^2\hat{s}.$$

The justification for this is the uniqueness theorem for the solution of the exterior form of the Neumann boundary value problem for Laplace's equation (Mikhlin 1970, p. 270).

7.1 Green's function for B_r

Outside the core we assume

$$\boldsymbol{B} = -\nabla\Omega,$$

$$\nabla^2\Omega = 0,$$

and

$$\Omega = O(r^{-2}), \qquad r \to \infty.$$

Then there is a spherical harmonic expansion for Ω starting at $l = 1$;

$$\Omega = c\sum_{l=1}^{\infty}\left(\frac{c}{r}\right)^{l+1}\sum_{m=-l}^{l} b_l^m Y_l^m(\theta, \phi), \tag{29}$$

and

$$B_r(r, \theta, \phi) = -\partial_r\Omega$$
$$= \sum_l\sum_m (l+1)\left(\frac{c}{r}\right)^{l+2} b_l^m Y_l^m(\theta, \phi), \tag{30}$$

where r, θ, and ϕ are the familiar spherical coordinates referred to Earth's centre and spin axis. Multiplying by $Y_{l'}^{m'*}$ and integrating over the core surface S, on which $r = c$, we get

$$\int_S B_r(c, \theta', \phi')Y_{l'}^{m'*}(\theta', \phi')d^2r'$$
$$= \sum_l\sum_m \int_S (l+1)b_l^m Y_l^m(\theta', \phi')Y_{l'}^{m'*}(\theta', \phi')d^2\hat{r}',$$

and by the orthogonality of the Y_l^m:

$$(l+1)b_l^m = \int_S B_r(c, \theta', \phi')Y_l^{m*}(\theta', \phi')d^2\hat{r}'. \tag{31}$$

Substituting expression (31) into (30) and then using the spherical harmonic addition theorem (Jackson 1963, p. 67) yields

$$B_r(r, \theta, \phi) = \int_S d^2\hat{r}' \sum_l\sum_m \left(\frac{c}{r}\right)^{l+2} Y_l^m(\theta, \phi)Y_l^{m*}(\theta', \phi')$$
$$\times B_r(c, \theta', \phi') = \int_S d^2\hat{r}' B_r(c, \theta', \phi')\sum_l \frac{2l+1}{4\pi}\left(\frac{c}{r}\right)^{l+2} P_l(\hat{r}'\cdot\hat{r}). \tag{32}$$

Now we make use of the generating function of Legendre polynomials

$$f = \frac{1}{(1+x^2-2x\mu)^{1/2}} = \sum_{l=0}^{\infty} x^l P_l(\mu)$$

$$2x\partial_x f = \sum_{l=0}^{\infty} 2lx^l P_l(\mu)$$

and

$$x^2(2x\partial_x f + f) = \sum_{l=0}^{\infty}(2l+1)x^{l+2}P_l(\mu).$$

The $l = 0$ term is subtracted yielding

$$\sum_{l=1}^{\infty}(2l+1)x^{l+2}P_l(\mu)$$
$$= x^2\left[\frac{-(2x^2-2x\mu)}{(1+x^2-2x\mu)^{3/2}} + \frac{1+x^2-2x\mu}{(1+x^2-2x\mu)^{3/2}}\right] - x^2$$
$$= \frac{x^2(1-x^2)}{(1+x^2-2x\mu)^{3/2}} - x^2.$$

Now letting $\rho = \frac{c}{r}$, $\mu = \cos\theta = \hat{r}\cdot\hat{r}'$, and $R = \sqrt{1-2\mu\rho+\rho^2}$ in (32) we get the required expression for $B_r(\boldsymbol{r})$ in terms of $B_r(\boldsymbol{s})$,

$$B_r(r, \theta, \phi) = \frac{1}{4\pi}\int_S d^2\hat{r}' B_r(c, \theta', \phi')\left[\frac{\rho^2(1-\rho^2)}{R^3} - \rho^2\right].$$

7.2 B_θ and B_ϕ

The horizontal components of the field are most easily obtained from the gradient of the potential function with respect to $\boldsymbol{r}$. We make use of the following identities, in which all gradients are with respect to $\boldsymbol{r}$.

$$\nabla(\boldsymbol{c}\cdot\boldsymbol{r}) = \boldsymbol{c}$$

$$\nabla(\boldsymbol{r}\cdot\boldsymbol{r}) = \nabla|\boldsymbol{r}|^2 = 2\boldsymbol{r}$$

$$\nabla\left(\frac{1}{|\boldsymbol{r}|}\right) = \nabla\frac{1}{\sqrt{|\boldsymbol{r}|^2}} = -\tfrac{1}{2}(|\boldsymbol{r}|^2)^{-3/2}2\boldsymbol{r} = -\frac{\hat{\boldsymbol{r}}}{|\boldsymbol{r}|^2}$$

$$\nabla[f(\boldsymbol{c}\cdot\boldsymbol{r})] = f'(\boldsymbol{c}\cdot\boldsymbol{r})\boldsymbol{c}$$

$$\nabla(\hat{r}\cdot\hat{r}') = \nabla\left(\frac{\boldsymbol{r}\cdot\hat{r}'}{|\boldsymbol{r}|}\right) = \frac{\hat{r}'}{|\boldsymbol{r}|} - \frac{\boldsymbol{r}\cdot\hat{r}'\hat{r}}{|\boldsymbol{r}|^2} = \frac{\hat{r}'-\mu\hat{r}}{r}.$$

Using (29) and (31) again we have

$$\boldsymbol{B} = -\nabla\Omega = -\nabla\frac{c}{4\pi}\int_S d^2\hat{r}' B_r(c, \theta', \phi')$$
$$\times\sum_l\left(\frac{c}{r}\right)^{l+1}\frac{2l+1}{l+1}P_l(\hat{r}\cdot\hat{r}').$$

Now with $\rho = \frac{c}{r}$, and $\mu = \hat{r}\cdot\hat{r}'$ as before, let

$$Q(\rho, \mu) = \sum_l \rho^{l+1}\frac{2l+1}{l+1}P_l(\mu).$$

We want

$$\nabla Q(\rho, \mu) = \sum_l \frac{2l+1}{l+1}\nabla\left[\left(\frac{c}{r}\right)^{l+1}P_l(\hat{r}\cdot\hat{r}')\right]$$
$$= \sum_l \frac{2l+1}{l+1}\left[-\frac{l+1}{c}\left(\frac{c}{r}\right)^{l+2}\hat{r}P_l(\hat{r}\cdot\hat{r}')\right.$$
$$\left. + \left(\frac{c}{r}\right)^{l+1}\nabla P_l(\hat{r}\cdot\hat{r}')\right]$$
$$= \sum_l \frac{2l+1}{l+1}\left[-\frac{l+1}{c}\left(\frac{c}{r}\right)^{l+2}\hat{r}P_l(\hat{r}\cdot\hat{r}')\right.$$
$$\left. + \left(\frac{c}{r}\right)^{l+1}P_l'(\hat{r}\cdot\hat{r}')\frac{\hat{r}'-\mu\hat{r}}{r}\right].$$

The first part of the sum is exactly what we had before for

the radial component of the field. For the second term we need to evaluate

$$\hat{r}' \sum_l \frac{2l+1}{l+1} \rho^{l+1} P_l'(\mu) = \frac{\hat{r}' - \mu\hat{r}}{r} \frac{\partial Q}{\partial \mu}$$

$$= \frac{\hat{r}' - \mu\hat{r}}{r} \frac{\rho^2(1+2R-\rho^2)}{R^3 T},$$

where once again $R = \sqrt{1-2\mu\rho+\rho^2}$ and $T = 1 + R - \mu\rho$. Making the appropriate substitutions yields the complete expression for the vector field in terms of the radial field on the core–mantle boundary:

$$\boldsymbol{B} = \frac{1}{4\pi} \int_S d^2\hat{r}' B_r(c, \theta', \phi') \times \left[\hat{r}\left[\frac{\rho^2(1-\rho^2)}{R^3} - \rho^2\right] - (\hat{r}' - \mu\hat{r})\rho^3 \frac{(1+2R-\rho^2)}{R^3 T}\right].$$

Taking dot products with the relevant unit vectors yields

$$B_\theta(r, \theta, \phi) = -\frac{1}{4\pi} \int_S d^2\hat{r}' B_r(c, \theta', \phi') \frac{(1+2R-\rho^2)}{R^3 T} \rho^3 \hat{r}' \cdot \hat{\theta},$$

and

$$B_\phi(r, \theta, \phi) = -\frac{1}{4\pi} \int_S d^2\hat{r}' B_r(c, \theta', \phi') \frac{(1+2R-\rho^2)}{R^3 T} \rho^3 \hat{r}' \cdot \hat{\phi}.$$